Progress In Electromagnetics Research, PIER 40, 295–314, 2003

A PRACTICAL APPROACH TO MODELING DOUBLY CURVED CONFORMAL MICROSTRIP ANTENNAS

C. A. Macon

High Performance Technologies, Inc.
PMB #134, 939-I Beards Hill Rd., Aberdeen, MD 21001, USA

K. D. Trott

Raytheon, Integrated Defense Systems
528 Boston post Rd., Sudbury, MA 01776, USA

L. C. Kempel

Department of Electrical and Computer Engineering
Michigan State University
East Lansing, MI 48824, USA

Abstract—Designers are increasingly integrating conformal microstrip antennas into the curved structures of either air or land vehicles. Quite often, these structures are doubly curved (e.g. curved along two orthogonal surface directions). This practice necessitates the development of accurate codes versatile enough to model conformal antennas with arbitrarily shaped apertures radiating from doubly curved surfaces. Traditional planar-structure-based design techniques are not well suited for this application. A hybrid finite element-boundary integral formulation appropriate for the high-frequency analysis and design of doubly curved conformal antennas is introduced in this paper. The novelty of this approach lies in its use of an asymptotic prolate spheroidal dyadic Green's function to model the physics of curved surface diffraction. To demonstrate the utility of this approach, the effects of curvature on the resonant frequency and input impedance of both a doubly curved conformal square and circular patch antenna are investigated. Different feed positions are also considered. Due to a paucity of published experimental data, the numerical results are benchmarked by comparison with the results for planar square and circular patch antennas. The planar results are obtained by using an experimentally validated planar finite element-boundary integral code.

1. INTRODUCTION

Designers are increasingly integrating conformal microstrip patch antennas into the curved structures of aircraft, satellites, and land vehicles due to functional or space constraints. Typically these structures are arbitrarilly shaped and doubly curved (e.g., exhibiting curvature along two orthogonal surface directions). It has been shown that planar models do not accurately predict the performance of nonplanar conformal patch antennas due to the effects of local curvature on their resonant frequency, input impedance, and radiation pattern [1, 2]. To be viable, design software must incorporate the effects of surface geometry in modeling the in situ performance of these antennas at high frequencies. Moreover, with the advent of wide bandwidth systems for high data rate transmission, design software must be versatile enough to model arbitrarily shaped apertures, such as log periodic and spiral antennas [3].

Modeling the high-frequency radiation patterns by arbitrarily shaped patch antennas conformal to doubly curved surfaces is not an easy task. Some common techniques that have been employed are transmission line model, cavity model, and full-wave numerical method [4]. The simple transmission line model is the easiest to implement; however, it is the least accurate and is restricted to rectangular patch geometries. Although the generalized transmission line model is more versatile, being applicable to patch shapes with separable geometries [4], it cannot accommodate arbitrary, nonseparable geometries. The cavity model is more versatile and accurate, but it is not amenable to microstrip antenna arrays [4]. The full-wave approach is undeniably the most rigorous and accurate technique for analyzing patch antennas. This approach relies upon the calculation of a closed-formed expression for the exact dyadic Green's function (DGF). The utility of this approach for planar geometries is well established; however, for

nonplanar geometries, there are some limitations. Although closed-form expressions for exact DGFs are derivable in cylindrical and spherical coordinates, they would converge poorly at high frequencies. Moreover, for reasons to be discussed in this paper, it may not be possible to derive a closed-form expression for an exact prolate spheroidal DGF.

In this paper, a practical approach to modeling doubly curved conformal microstrip patch antennas with arbitrarily shaped apertures, based on the hybrid finite element-boundary integral method (FE-BI), is presented. In this formulation, a prolate spheroid is chosen to canonically model a general convex doubly curved surface. This shape is general in that it exhibits constant and variable curvatures along azimuthally and axially oriented orthogonal surface directions, respectively. By the appropriate specification of its radii of curvature, convex surfaces of arbitrary curvature can be modeled. In addition, the canonical cylindrical and spherical surfaces may be recovered as limiting cases. It is shown that the physics of high-frequency surface diffraction by doubly curved surfaces is intrinsic to an asymptotic approximation to a prolate spheroidal second-kind electric DGF. This DGF may be physically interpreted as the surface diffracted field (e.g., creeping waves) excited by an infinitesimal magnetic dipole on the surface of a perfect electrically conducting (PEC) prolate spheroid. Numerical results for the resonant frequencies and input impedance of conformal doubly curved cavity-backed square and circular patch antennas are presented. To demonstrate the utility of this approach, the effects of surface curvature variation on the input impedance for various antenna orientations and probe feed positions are investigated. Due to a paucity of published experimental data for doubly curved patch antennas, the numerical results are benchmarked by comparisons with the experimentally confirmed numerical results for planar patch antennas.

2. FORMULATION OF A FULL-WAVE SOLUTION

A prolate spheroid is generated by rotating an ellipse about its major semi-axis. The prolate spheroidal coordinate system, as depicted in Figure 1, is defined in terms of the rectangular coordinate system by

$$\begin{aligned} x &= F\sqrt{(\xi^2-1)(1-\eta^2)}\cos\varphi \\ y &= F\sqrt{(\xi^2-1)(1-\eta^2)}\sin\varphi \\ z &= F\xi\eta \end{aligned} \tag{1}$$

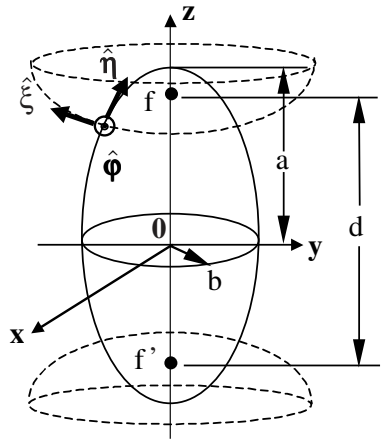

Figure 1. Prolate spheroidal geometry.

where the semi-interfocal distance, F, is given by $F = d/2$ and

$$\begin{aligned} -1 \leq \eta \leq 1 \\ 1 \leq \xi \leq \infty \\ 0 \leq \varphi \leq 2\pi \end{aligned} \tag{2}$$

are the coordinate constraints. Referencing Figure 1, a is an axial length parameter and b is the azimuthal radius of curvature. The ordered triple (η, ξ, φ) forms a right-handed coordinate system. The scalar Helmholtz equation given by

$$(\nabla^2 + k^2)\psi = 0 \tag{3}$$

can be written as

$$\frac{\partial}{\partial\eta}\left[(1-\eta^2)\frac{\partial\psi}{\partial\eta}\right]+\frac{\partial}{\partial\xi}\left[(\xi^2-1)\frac{\partial\psi}{\partial\xi}\right]+\frac{\xi^2-\eta^2}{(1-\eta^2)(\xi^2-1)}\frac{\partial^2\psi}{\partial\varphi^2}+c^2(\xi^2-\eta^2)\psi=0 \tag{4}$$

in the prolate spheroidal coordinate system, where $c = kF$ and $k = 2\pi/\lambda$. The scalar Helmholtz equation in (4) is separable with the solution given by

$$\psi^{(h)}_{\binom{e}{o}mn} = S^{(1)}_{mn}(c,\eta)R^{(h)}_{mn}(c,\xi)\begin{pmatrix}\cos m\varphi \\ \sin m\varphi\end{pmatrix}. \tag{5}$$

In (5), the angular function of the first kind, denoted by $S^{(1)}_{mn}(c,\eta)$, is

given by

$$S_{mn}^{(1)}(c,\eta) = \sum_{r=0,1}^{\infty'} d_r^{mn}(c) P_{m+r}^m(\eta) \tag{6}$$

where $m \geq 0$ and $n \geq m$ are integers, the prime indicates a summation over even r for $n-m$ even and over odd r for $n-m$ odd, $P_{m+r}^m(\eta)$ is the associated Legendre polynomial, and $d_r^{mn}(c)$ are the expansion coefficients. The angular function of the second kind is not used, since it is not regular over the range of η. The radial function, denoted by $R_{mn}^{(h)}(c,\xi)$, is given by

$$R_{mn}^{(h)}(c,\xi) = \frac{1}{\alpha}\left(\frac{\xi^2-1}{\xi^2}\right)^{\frac{m}{2}} \sum_{r=0,1}^{\infty'} (j)^{r+m-n} d_r^{mn}(c) \frac{(2m+r)!}{r!} z_{m+r}^{(h)}(c\xi) \tag{7}$$

where

$$\alpha = \sum_{r=0,1}^{\infty'} d_r^{mn}(c) \frac{(2m+r)!}{r!} \tag{8}$$

and $z_{m+n}^{(h)}(c\xi)$ denotes the spherical Bessel function, Neumann, or Hankel functions of the first or second kind, for $h = 1, 2, 3$, and 4 respectively. The superscript $h = 4$ denotes outgoing waves under the $e^{j\omega t}$ time convention, which is used throughout this paper. Applying the following vector differential operators to the general solution in (5)

$$\begin{aligned} \mathbf{M}_q^{(h)} &= \nabla \psi_q^{(h)} \times \mathbf{a} \\ \mathbf{N}_q^{(h)} &= \frac{1}{k} \nabla \times \mathbf{M}_q^{(h)} \end{aligned} \tag{9}$$

and setting the pilot vector $\mathbf{a}$ equal to the position vector $\mathbf{r}$, expressions for the spheroidal vector wave functions $\mathbf{M}$ and $\mathbf{N}$ are obtained. Thus, the components of $\mathbf{M}$ are given by

$$\begin{aligned} {}^r M_{q\eta}^{(h)} &= \frac{m\xi}{\sqrt{(\xi^2-\eta^2)(1-\eta^2)}} S_{mn}^{(1)}(c,\eta) R_{mn}^{(h)}(c,\xi) \begin{pmatrix} \sin m\varphi \\ -\cos m\varphi \end{pmatrix} \\ {}^r M_{q\xi}^{(h)} &= \frac{m\eta}{\sqrt{(\xi^2-\eta^2)(\xi^2-1)}} S_{mn}^{(1)}(c,\eta) R_{mn}^{(h)}(c,\xi) \begin{pmatrix} -\sin m\varphi \\ \cos m\varphi \end{pmatrix} \\ {}^r M_{q\varphi}^{(h)} &= \frac{\sqrt{(\xi^2-1)(1-\eta^2)}}{\xi^2-\eta^2} \left[\xi \frac{d}{d\eta} S_{mn}^{(1)}(c,\eta) R_{mn}^{(h)}(c,\xi) \right. \\ &\quad \left. - \eta S_{mn}^{(1)}(c,\eta) \frac{d}{d\xi} R_{mn}^{(h)}(c,\xi)\right] \begin{pmatrix} \cos m\varphi \\ \sin m\varphi \end{pmatrix} \end{aligned} \tag{10}$$

and those of **N** are given by

$$
\begin{aligned}
{}^{r}N_{q\eta}^{(h)} = \frac{1}{kF}\frac{\sqrt{1-\eta^2}}{\sqrt{\xi^2-\eta^2}}\Bigg\{ & \frac{d}{d\eta}S_{mn}^{(1)}(c,\eta)\frac{\partial}{\partial\xi}\left[\frac{\xi(\xi^2-1)}{\xi^2-\eta^2}R_{mn}^{(h)}(c,\xi)\right] \\
& -\eta S_{mn}^{(1)}(c,\eta)\frac{\partial}{\partial\xi}\left[\frac{\xi^2-1}{\xi^2-\eta^2}\frac{d}{d\xi}R_{mn}^{(h)}(c,\xi)\right] \\
& + \frac{m^2\eta}{(1-\eta^2)(\xi^2-1)}S_{mn}^{(1)}(c,\eta)R_{mn}^{(h)}(c,\xi)\Bigg\}\begin{pmatrix}\cos m\varphi\\ \sin m\varphi\end{pmatrix} \qquad (11)
\end{aligned}
$$

$$
\begin{aligned}
{}^{r}N_{q\xi}^{(h)} = \frac{1}{kF}\frac{\sqrt{\xi^2-1}}{\sqrt{\xi^2-\eta^2}}\Bigg\{ & \frac{\partial}{\partial\eta}\left[\frac{\eta(1-\eta^2)}{\xi^2-\eta^2}S_{mn}^{(1)}(c,\eta)\right]\frac{d}{d\xi}R_{mn}^{(h)}(c,\xi) \\
& -\xi\frac{\partial}{\partial\eta}\left[\frac{1-\eta^2}{\xi^2-\eta^2}\frac{d}{d\eta}S_{mn}^{(1)}(c,\eta)\right]R_{mn}^{(h)}(c,\xi) \\
& + \frac{m^2\xi}{(1-\eta^2)(\xi^2-1)}S_{mn}^{(1)}(c,\eta)R_{mn}^{(h)}(c,\xi)\Bigg\}\begin{pmatrix}\cos m\varphi\\ \sin m\varphi\end{pmatrix} \qquad (12)
\end{aligned}
$$

$$
\begin{aligned}
{}^{r}N_{q\varphi}^{(h)} = \frac{m}{kF}\frac{\sqrt{(\xi^2-1)(1-\eta^2)}}{\xi^2-\eta^2}\Bigg\{ & \frac{1}{\xi^2-1}\frac{d}{d\eta}\left[\eta S_{mn}^{(1)}(c,\eta)\right]R_{mn}^{(h)}(c,\xi) \\
& + \frac{1}{1-\eta^2}S_{mn}^{(1)}(c,\eta)\frac{d}{d\xi}\left[\xi R_{mn}^{(h)}(c,\xi)\right]\Bigg\}\begin{pmatrix}-\sin m\varphi\\ \cos m\varphi\end{pmatrix} \qquad (13)
\end{aligned}
$$

where the preceding superscript r denotes that **M** and **N** were derived using the **r** pilot vector and $q = \binom{e}{o} mn$.

3. DRAWBACKS TO THE FULL-WAVE APPROACH

In this section, the problems with the full-wave solution for the prolate spheroidal geometry are discussed. The most critical problems are fundamental and are gleaned from a closer examination of the mathematical properties of the spheroidal vector wave functions. By analogy to the spherical coordinate system, one would surmise that the radial unit vector, $\hat{\xi}$, could be used as a piloting vector. However, a caveat of using $\hat{\xi}$ as the pilot vector is that the resulting vector wave functions do not satisfy the vector Helmholtz equation [5]. Moreover, a formulation, which employs the position vector, **r**, as the pilot vector, yields vector wave functions that are neither self nor mutually orthogonal [6]. Perhaps the most serious mathematical limitation is that the spheroidal vector wave functions are inherently only capable of modeling azimuthally symmetric (e.g., independent of φ) fields. If $\nabla \times \mathbf{r}\psi$ represents the electric field, the boundary conditions require

the tangential η and φ field components to vanish on the PEC spheroid surface. However, as Spence and Wells [7] have rigorously shown, this requirement can only be met by the $\mathbf{M}$ and $\mathbf{N}$ functions for the limiting cases of azimuthal invariance or for the degenerate case of ξ equal to zero. Analogous statements can be made about $\nabla \times \nabla \times \mathbf{r}\psi$. This is because $\nabla \times \mathbf{r}\psi$ and $\nabla \times \nabla \times \mathbf{r}\psi$ contain all field components [7]. The implications of this are far-reaching. From these properties, it appears that the derivation of an exact analytical closed-form expression for the DGF utilizing $\mathbf{M}$ and $\mathbf{N}$ for azimuthally asymmetric fields, is an analytically intractable problem.

The expressions for the DGF, comprised of analytically complicated series expressions for $S_{mn}^{(1)}(c,\eta)$, $R_{mn}^{(h)}(c,\eta)$, and the spheroidal vector wave functions given by (10)–(13), are quite cumbersome to compute. Like the other more familiar functions of mathematical physics (e.g., Bessel and Legendre functions) the spheroidal functions are poorly convergent for large arguments (large argument could be frequency or electrical size as a function of frequency) due to the large number of series terms needed for reasonable accuracy. This problem is compounded by the aforementioned complexities of $S_{mn}^{(1)}(c,\eta)$, $R_{mn}^{(h)}(c,\eta)$ $\mathbf{M}$, and $\mathbf{N}$. Specifically, the unknown scattering coefficients needed to calculate the exact DGF in (14) must be determined by solving a simultaneous system of coupled equations comprising infinite series. These infinite series must be truncated; however, the truncation number is proportional to the largest dimension, a, of the spheroid [8]. Thus, in addition to the large number of series terms needed to compute the spheroidal wave functions for an electrically large prolate spheroid, a large number of series terms would also be needed to accurately compute the scattering coefficients. Therefore, the costs associated with the numerical computation of an exact DGF at high frequencies could be prohibitive and would probably not converge due to the size of the prolate spheroid.

One possible approach for computing the expansion coefficients would be to express the second-kind electric DGF, denoted by $\overline{\overline{\mathbf{G}}}_{e2}$, in the form [9]

$$\overline{\overline{\mathbf{G}}}_{e2}(\mathbf{r}|\mathbf{r}') = \sum_m \sum_n \left[A_{qp}^M(\mathbf{r}')\, {}^r\mathbf{M}_{qp}^I(\mathbf{r})\, {}^r\mathbf{M}_{qp}^{I\,\prime}(\mathbf{r}) + A_{qp}^N(\mathbf{r}')\, {}^r\mathbf{N}_{qp}^I(\mathbf{r})\, {}^r\mathbf{N}_{qp}^{I\,\prime}(\mathbf{r}) \right] \tag{14}$$

where

$$\begin{aligned} {}^r\mathbf{M}_{qp}^I(\mathbf{r}) &= {}^r\mathbf{M}_{qp}^{(1)}(\mathbf{r}) + \alpha_p^r \mathbf{M}_{qp}^{(4)}(\mathbf{r}) \\ {}^r\mathbf{N}_{qp}^I(\mathbf{r}) &= {}^r\mathbf{N}_{qp}^{(1)}(\mathbf{r}) + \beta_p^r \mathbf{N}_{qp}^{(4)}(\mathbf{r}) \end{aligned} \tag{15}$$

and $p = \xi, \eta, \varphi$. The expansion coefficients $A_{qp}^{M}(\mathbf{r}')$ and $A_{qp}^{N}(\mathbf{r}')$ would then be determined numerically such that $\overline{\overline{\mathbf{G}}}_{e2}$ satisfies the Neumann boundary condition on the spheroid surface.

4. FE-BI FORMULATION

The FE-BI formulation in terms of the total electric field begins with the weak form of the vector wave equation followed by the specification of appropriate vector finite elements, expansion functions, and DGF. The reader is referred to [10] for details. The discretized FE-BI equation is given by

$$\sum_{j=1}^{N} E_j \left[\begin{array}{l} \displaystyle\int_V \left\{ \nabla \times \mathbf{W}_i \cdot \overline{\overline{\mu}}_r^{-1} \cdot \nabla \times \mathbf{W}_j - k_0^2 \mathbf{W}_i \cdot \overline{\overline{\varepsilon}}_r \cdot \mathbf{W}_j \right\} dV - \\ \displaystyle k_0^2 \int_{S_i} \int_{S_j} (\hat{\xi} \times \mathbf{W}_i) \cdot \overline{\overline{\mathbf{G}}}_{e2}(\xi_0, \theta, \varphi | \theta', \varphi') \cdot (\hat{\xi}' \times \mathbf{W}_j) dS' dS \end{array} \right] = f_i^{\text{int}} + f_j^{ext} \quad (16)$$

where E_j is the unknown complex coefficient associated with a free edge of the volumetric mesh and $\xi = \xi_0$ at the surface. A free edge is any edge that is not tangential to a PEC surface; the expansion coefficient of a tangential edge is zero. The total number of free edges is denoted by N. Galerkin's testing procedure is used; whereby, the constant tangential/linear normal (CT/LN) vector testing and expansion functions, given by $\mathbf{W}_i$ and $\mathbf{W}_j$, respectively, are identical. These expansion functions correspond to the shape functions used with tetrahedral elements. The free-space wavenumber is given by $k_0 = 2\pi/\lambda_0$ and the relative anisotropic permeability and permittivity denoted by $\overline{\overline{\mu}}_r$ and $\overline{\overline{\varepsilon}}_r$, respectively, are allowed to vary on a per-element basis. The DGF, $\overline{\overline{\mathbf{G}}}_{e2}$, will be discussed in detail later. The interior excitation functional is given by

$$f_i^{\text{int}} = -jk_0 Z_0 \int_V \mathbf{W}_i \cdot \mathbf{J}^{\text{int}} dV \quad (17)$$

while the exterior excitation functional is given by

$$f_i^{ext} = jk_0 Z_0 \int_S \mathbf{W}_i \cdot \hat{\xi} \times \left(\mathbf{H}^{inc} + \mathbf{H}^{ref} \right) dS \quad (18)$$

where $\hat{\xi}$ is the aforementioned unit normal vector in prolate spheroidal coordinates, Z_0 is the free-space impedance, $\mathbf{H}^{inc}$ is the incident field, $\mathbf{H}^{ref}$ is the reflected field, and $\mathbf{J}^{\text{int}}$ is the excitation current. The exact

condition for mesh truncation is enforced by the boundary integral via the DGF. The DGF couples the tangential electric and magnetic fields in the aperture and enforces the boundary condition on the tangential electric field at the PEC spheroid surface. Hence, the boundary integral has support only over the nonmetallic parts of the surface. This minimizes the number of surface unknowns thereby reducing the computational burden.

The utilization of an asymptotic second-kind electric DGF circumvents the problems inherent in an exact formulation that were discussed previously. As mentioned previously, the asymptotic DGF is derived within the context of a uniform theory of diffraction (UTD) formalism developed by Pathak and Kouyoumjian [11]. In order to derive the asymptotic DGF, a closed-form expression for tracing geodesic paths on prolate spheroids is needed. For convenience, the surface may be parameterized in terms of the spherical coordinates θ and φ via:

$$x = b\sin\theta\cos\varphi \tag{19}$$

$$y = b\sin\theta\sin\varphi \tag{20}$$

$$z = a\cos\theta \tag{21}$$

where a and b are the axial length parameter and azimuthal radius of curvature, respectively, as shown in Figure 1. The calculus of variations may then be used to determine the extremum of the arc length between two points on the surface. This leads to an expression for a geodesic, which is given by

$$\varphi(\theta) = \int \frac{\left(a^2\sin^2\theta + b^2\cos^2\theta\right)^{1/2} c_1}{b\sin\theta\left(b^2\sin^2\theta - c_1^2\right)^{1/2}} d\theta + c_2 \tag{22}$$

where c_1 and c_2 are integration constants that must be determined by specifying the starting and ending points of the geodesic [12]. The geodesic path length can now be computed and is given by [12]

$$s = \int_{\theta_s}^{\theta_d} \frac{b\sin\theta\left(a^2\sin^2\theta + b^2\cos^2\theta\right)^{1/2}}{\left(b^2\sin^2\theta - c_1^2\right)^{1/2}} d\theta. \tag{23}$$

Another required parameter is the geodesic angle δ. This is the angle subtended from the azimuthal plane of the prolate spheroid to a line tangent to the geodesic trajectory; it is given by

$$\delta = \sin^{-1}\left(\frac{c_1}{b\sin\theta}\right). \tag{24}$$

Another parameter that is essential to the UTD formulation is the generalized Fock distance parameter β, which is given by

$$\beta = \left(\frac{k_0}{2}\right)^{1/3} \int_{\theta_s}^{\theta_d} \frac{\left(a\left[b^4 + c_1^2\{a^2 - b^2\}\right]\right)^{2/3} \sin\theta}{b\left(\left[a^2\sin^2\theta + b^2\cos^2\theta\right]\left[b\sin\theta - c_1^2\right]\right)^{1/2}} d\theta. \quad (25)$$

Furthermore, it can be shown by the use of differential geometry that φ = constant and η = constant define orthogonal curves along the surface. The basis vectors, $\hat{\boldsymbol{\varphi}}$ and $\hat{\boldsymbol{\eta}}$, aligned in parallel with the orthogonal surface curves, form the basis of an orthogonal coordinate system. Consequently, the expressions for the ray-based unit tangent, normal and binormal vectors $(\hat{\mathbf{t}}, \hat{\mathbf{n}}, \hat{\mathbf{b}})$ may be determined. Having defined the surface geodesic coordinate system, we can now calculate the radii of curvature along the principal surface directions $\hat{\boldsymbol{\eta}}$ and $\hat{\boldsymbol{\varphi}}$, respectively, of the spheroid. They are given by the following

$$\rho_1 = \frac{\left(a^2\sin^2\theta + b^2\cos^2\theta\right)^{3/2}}{ab} \quad (26)$$

and

$$\rho_2 = \frac{b\left(a^2\sin^2\theta + b^2\cos^2\theta\right)^{1/2}}{a}. \quad (27)$$

Once the radii of curvature have been determined, the geodesic radius of curvature can also be found using differential geometry, and it is given by

$$\rho_g = \frac{b^3\sin^2\theta\left(a^2\sin^2\theta + b^2\cos^2\theta\right)^{3/2}}{a\left(b^2\left[b^2\sin^2\theta - c_1^2\right] + c_1^2\left[a^2\sin^2\theta + b^2\cos^2\theta\right]\right)}. \quad (28)$$

Now that the principal radii of curvature, ρ_1 and ρ_2, and the geodesic curvature, ρ_g, have been determined, it is a straightforward task to calculate the remaining ray parameters; namely, the torsion τ, torsion factor τ_0, and interpolating factors γ_c and γ_s. Following the UTD formalism in [11], expressions for the dyadic components are given by [12]

$$\begin{aligned} G_{e2}^{\varphi\varphi}(\theta,\varphi|\theta',\varphi') = \Big\{ & (\cos^2\delta(\theta) - q[(D^2+2)\cos^2\delta(\theta) - (D^2+1)])v(\beta) \\ & + q^2([D^2+2]\cos^2\delta(\theta) - 2)[\gamma_s u(\beta) + \gamma_c v(\beta)] \\ & + (\tau_o\cos\delta(\theta) + \sin\delta(\theta))^2 q[u(\beta) - v(\beta)]\Big\} D\frac{k_o^2 Y_o}{2\pi} q e^{-jk_o s} \end{aligned} \quad (29)$$

$$G_{e2}^{\eta\varphi} = G_{e2}^{\varphi\eta}(\theta,\varphi|\theta',\varphi') = \Big\{-\sin\delta(\theta)\cos\delta(\theta)(v(\beta)-(D^2+2)qv(\beta) +(D^2+2)q^2[\gamma_s u(\beta)+\gamma_c v(\beta)]) + [(2\cos^2\delta(\theta)-1)\tau_o - (\tau_o^2-1)\sin\delta(\theta)\cos\delta(\theta)]q[u(\beta)-v(\beta)]\Big\}\frac{k_o^2 Y_o}{2\pi}qe^{-jk_o s} \quad (30)$$

$$G_{e2}^{\eta\eta}(\theta,\varphi|\theta',\varphi') = \Big\{(\sin^2\delta(\theta)-q[(D^2+2)\sin^2\delta(\theta)-(D^2+1)])v(\beta) +q^2([D^2+2]\sin^2\delta(\theta)-2)[\gamma_s u(\beta)+\gamma_c v(\beta)] +(\tau_o\sin\delta(\theta)-\cos\delta(\theta))^2 q[u(\beta)-v(\beta)]\Big\}D\frac{k_o^2 Y_o}{2\pi}qe^{-jk_o s} \quad (31)$$

where $q = \frac{j}{k_0 s}$, $u(\beta)$, and $v(\beta)$ are the soft and hard surface Fock functions, respectively. The Fock functions mathematically quantify the attenuation of creeping waves propagating along curved geodesic paths on the surface. The surface ray divergence factor, D, which quantifies the spread in width of a surface diffracted ray as it sheds rays, is determined numerically in this application. The geodesic coordinates of the ray source and shedding points are denoted by (θ',φ') and (θ,φ), respectively. With the substitution of the components in (29)–(31) into the following expression

$$\overline{\overline{\mathbf{G}}}_{e2}(\xi_0,\theta,\varphi|\theta',\varphi') = \hat{\boldsymbol{\varphi}}\hat{\boldsymbol{\varphi}}G_{e2}^{\varphi\varphi}(\theta,\varphi|\theta',\varphi') + \hat{\boldsymbol{\varphi}}\hat{\boldsymbol{\eta}}'G_{e2}^{\varphi\eta}(\theta,\varphi|\theta',\varphi') +\hat{\boldsymbol{\eta}}\hat{\boldsymbol{\varphi}}'G_{e2}^{\eta\varphi}(\theta,\varphi|\theta',\varphi') + \hat{\boldsymbol{\eta}}\hat{\boldsymbol{\eta}}'G_{e2}^{\eta\eta}(\theta,\varphi|\theta',\varphi') \quad (32)$$

the asymptotic DGF is now in a form that is suitable for substitution into the boundary integral in (16).

Geodesic curves, traced by numerically integrating (22), are shown in Figures 2(a) and 2(b). Figure 2(a) depicts a geodesic curve along the midsection of a $40.0 \times 4.0\lambda$ prolate spheroid. In this region, the curvature profile of the spheroid may be regarded as quasicylindrical. In Figure 3(a), the magnitudes of the prolate spheroidal asymptotic DGF components as functions of the electrical geodesic path length along the geodesic in Figure 2(a) are given. As expected, there is uniform attenuation along this path, which agrees quite well with the attenuation of the cylindrical asymptotic DGF components along a geodesic curve with the same orientation along a circular cylinder whose radius is the same. A geodesic curve near the tip of a $40.0\times4.0\lambda$ prolate spheroid is depicted in Figure 2(b). In Figure 3(b), the magnitudes of the spheroidal asymptotic DGF components along the

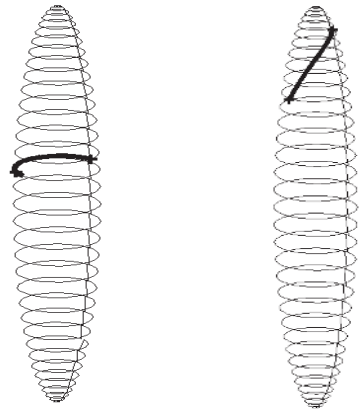

(a) (b)

Figure 2. Geodesic paths along a prolate spheroid.

geodesic depicted in Figure 2(b) are given. As expected, the magnitude of the $\hat{\boldsymbol{\eta}}\hat{\boldsymbol{\eta}}$-component exhibits the greatest non-uniformity, varying as a function of position along the geodesic, due to curvature variation along the axial direction.

Now that the finite element and boundary integral equations have been specified, the FE-BI equation may be solved. The FE-BI equation in (16) may be rewritten in matrix form as

$$\begin{bmatrix} A_{aa} & A_{ai} \\ A_{ia} & A_{ii} \end{bmatrix} \begin{bmatrix} E^{ap} \\ E^{\text{int}} \end{bmatrix} + \begin{bmatrix} G & 0 \\ 0 & 0 \end{bmatrix} \begin{bmatrix} E^{ap} \\ E^{\text{int}} \end{bmatrix} = \begin{bmatrix} 0 \\ f^{\text{int}} \end{bmatrix} \tag{33}$$

where $[A]$ is the finite element matrix, $[G]$ is the boundary integral sub-matrix, E^{int} is the unknown electric field in the cavity, E^{ap} is the unknown electric field in the aperture, and f^{int} denotes the interior excitation due to the probe feed. The decomposition of the FE-BI matrix in this manner allows the matrix-vector product in each partition to be optimized for solution by an iterative solver. As an example, since the finite element matrix is sparse, the matrix can be stored in an efficient compressed sparse row fashion [13] and the matrix-vector multiplication scheme can be optimized for a sparse matrix. Since the boundary integral matrix is symmetric, only the upper (or lower) triangle needs to be stored. Hence, the matrix-vector multiplication can be optimized for a symmetric matrix.

Once the electric fields in the cavity $\mathbf{E}^{\text{int}}$ and in the aperture $\mathbf{E}^{ap}$ have been found by solving using a suitable iterative solver such as the biconjugate gradient (BiCG) method, the input impedance can be

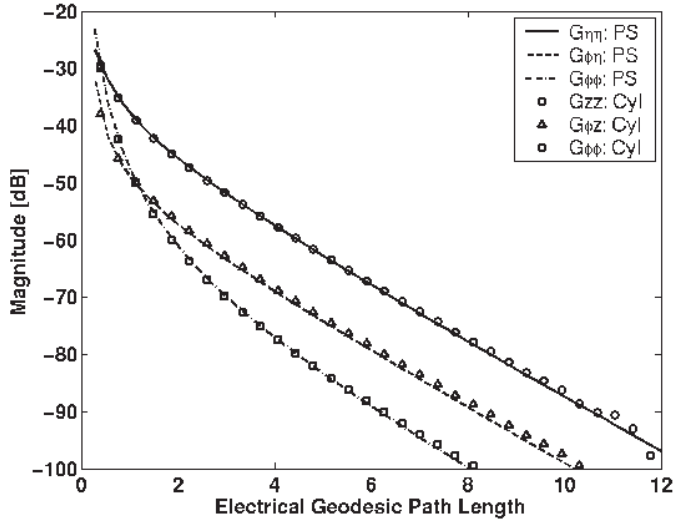

(a)

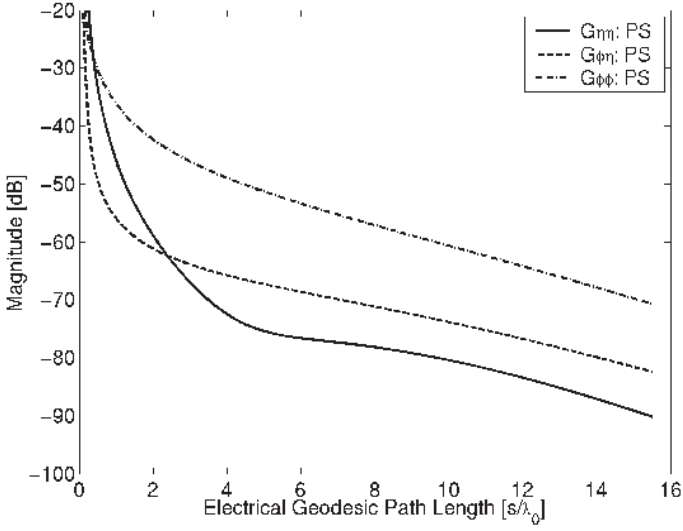

(b)

Figure 3. Magnitudes of the prolate spheroidal asymptotic dyadic Green's function components along the geodesic paths in Figs. 2(a) (midsection) and 2(b) (near the tip), respectively.

found. The input impedance is calculated from the ratio of the voltage at the input port to the current flowing into the port. The simplest feed is a Hertzian dipole where the source is a filament of current. For this case, the input impedance can be computed using Gauss' Law

$$Z_{in} = \frac{1}{I_{in}} \sum_{n=1}^{6} E_{j(n)} \int \hat{\mathbf{I}} \cdot \mathbf{W}_{j(n)} dl' \tag{34}$$

where $\hat{\mathbf{I}}$ denotes the orientation of the probe-feed. The total electric field at the feed location is determined by summing over all the edges of the element, which would be the six edges of the tetrahedral containing the probe-feed in this case, and integrating over the length of the probe. Since this approach relies upon an accurate field calculation in the vicinity of the feed, it is important to finely sample the computational volume in the vicinity of the feed.

5. NUMERICAL RESULTS OF THE FE-BI SOLUTION

In the preceding sections, the FE-BI formulation appropriate for modeling conformal antennas flush-mounted on doubly curved surfaces has been presented. In this section, the behavior of the input impedance of a cavity-backed, conformal square and a circular patch antenna for various curvatures and probe feed positions are investigated by using the FE-BI method. Although published data on waveguide antennas flush-mounted on doubly curved surfaces is becoming available [14], published data on the effect of doubly curved surface curvature variation on the input impedance of cavity-backed patch antennas are quite scarce. Nevertheless, the results for the input impedances of doubly curved conformal antennas will be benchmarked against the input impedance results from an experimentally confirmed planar tetrahedral-based FE-BI code [15].

First, a square patch antenna is considered. The antenna consists of a 2.5 cm by 2.5 cm square, metallic patch printed on a 30-mil substrate situated in a square aperture of 5.0 cm by 5.0 cm. The substrate is composed of a dielectric material with a complex permittivity of $3.2–j0.045$. The conformal finite element mesh for this antenna is shown in Figure 4. By analogy to the singly curved case, an axially polarized electric field normal to the spheroid surface is excited by a probe feed that is positioned on an axially oriented centerline along the patch. The electric field configuration for this polarization state at the resonant frequency is shown in Figure 5(a). From an examination of the input impedance spectrum for this polarization state, depicted in Figure 6(a), it is apparent that the resonant

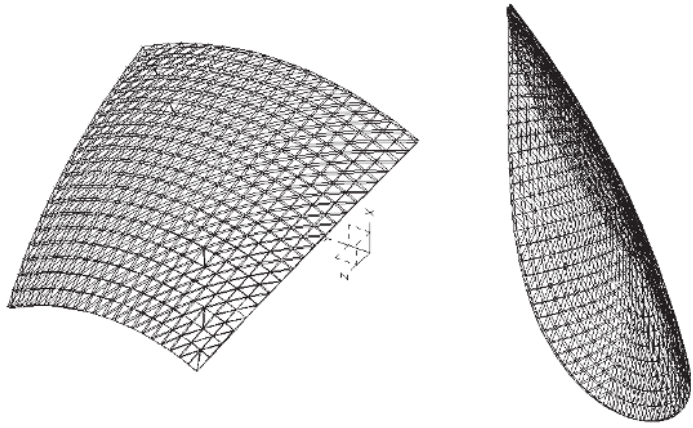

Figure 4. Finite element meshes of the conformal square and circular patch antennas.

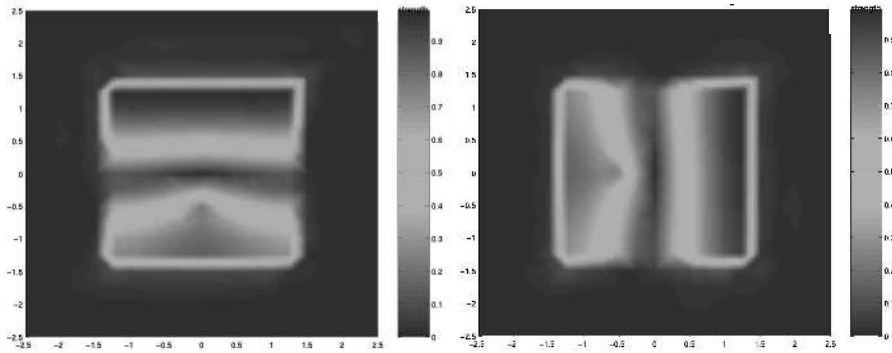

(a) (b)

Figure 5. Electric field beneath the conformal square patch antenna for axial (a) and azimuthal (b) polarizations.

frequency is practically independent of surface curvature. Conversely, a probe feed positioned along an azimuthally oriented centerline excites an azimuthally polarized electric field. The electric field configuration and input impedance spectrum for this polarization state at the resonant frequency are shown in Figure 5(b) and 6(b), respectively. For the azimuthal polarization as compared to the axial polarization, the resonant frequency exhibits a higher degree of curvature dependence.

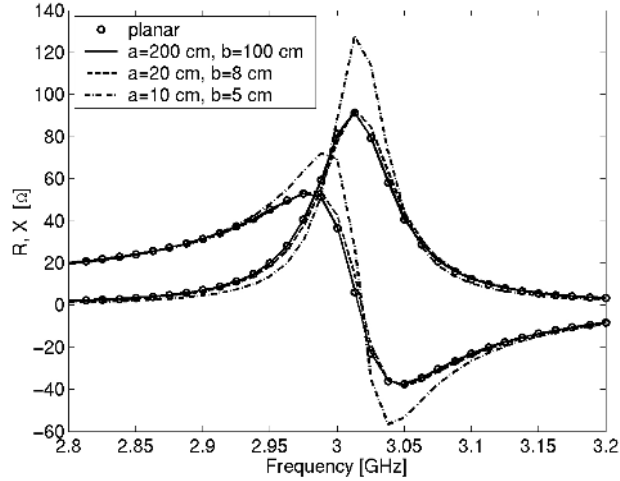

(a)

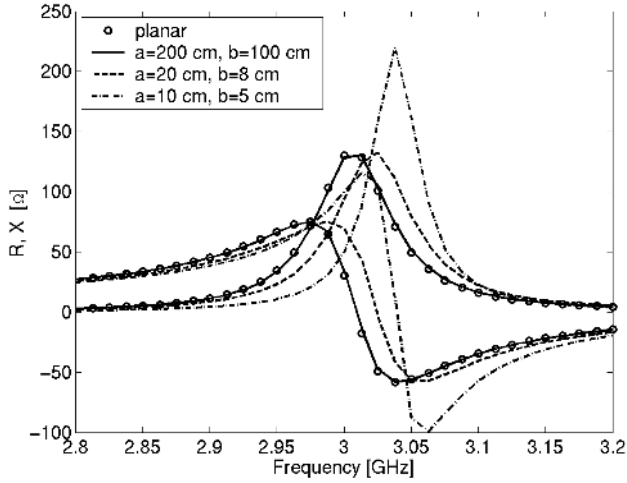

(b)

Figure 6. Curvature dependence of the input impedance of the conformal square patch antenna for axial (a) and azimuthal (b) polarizations. The feed positions are indicated in the insets.

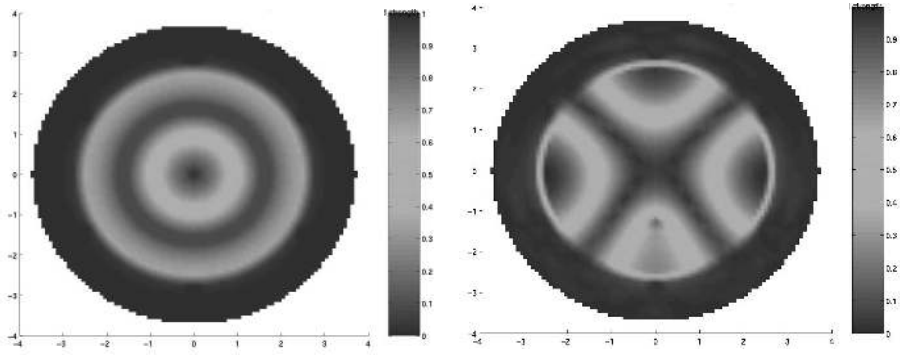

(a) (b)

Figure 7. Electric field beneath the conformally circular patch excited by a centrally located (a) and an off-centered (b) probe feed.

This result seems quite reasonable due to the relatively high degree of curvature along the azimuthal as opposed to the axial direction. By specifying a prolate spheroid with electrically large azimuthal and axial radii of curvature, these results are benchmarked by comparison with the results obtained for the input impedance of a planar square patch antenna excited at the same feed location. The surface of an electrically large prolate spheroid may be regarded as locally planar in the vicinity of the patch. As seen in Figure 6(b), this also leads to an input impedance spectrum that agrees quite well with the corresponding planar value.

Next, we consider a conformally circular patch antenna. The circular patch antenna consists of a metallic patch of radius 2.5 cm within an aperture of radius 3.75 cm. The finite element mesh generated for this antenna is shown in Figure 4. The permittivity of the substrate is the same as that of the square patch. The resonant electric field excited by a probe at the center of the patch is shown in Figure 7(a). The input impedance spectrum for this polarization, as shown in Figure 8(a), exhibits slight curvature dependence. An off-centered probe feed excites multiple modes with a resonant electric field structure shown in Figure 7(b). From an examination of the input impedance spectrum in Figure 8(b), it is evident that the resonant frequencies of these modes are sensitive to the surface curvature variation. Just as before, these results are validated by comparison with the results obtained from the planar tetrahedral code for a planar circular patch.

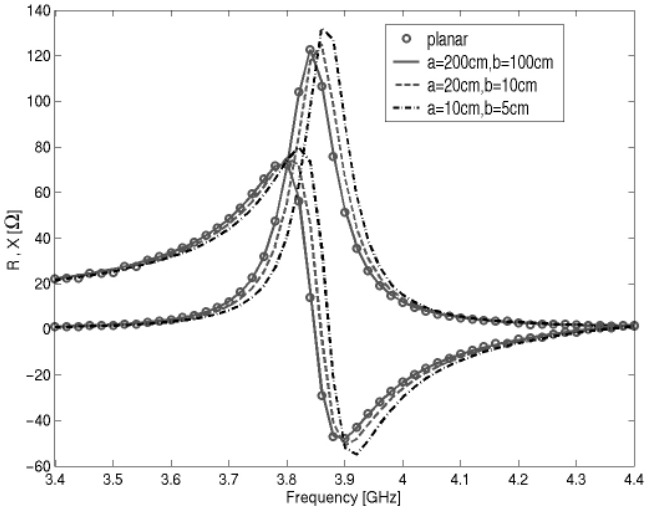

(a)

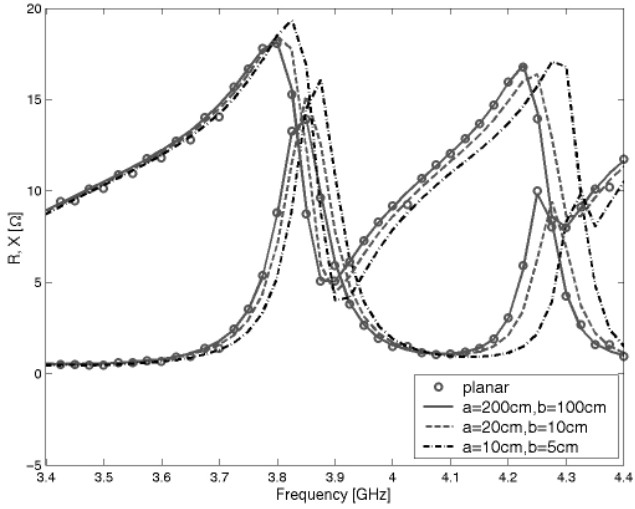

(b)

Figure 8. Curvature dependence of the input impedance of the conformally circular patch antenna corresponding to (a) the feed position in Fig. 7(a) and (b) the feed position in Fig. 7(b). The feed positions are indicated in the insets.

6. CONCLUSIONS

An FE-BI formulation appropriate for modeling cavity-backed doubly curved conformal antennas with arbitrarily shaped apertures has been presented. Since a prolate spheroid can recover the canonical cylindrical and spherical surfaces as limiting cases through a suitable choice of its radii of curvature, it is sufficiently general to model an arbitrary doubly curved surface. The disadvantages of a full-wave solution for prolate spheroidal geometries were discussed and served to justify the use of an asymptotic approach to modeling the physics of curved surface diffraction. To demonstrate the utility of this approach, the effects of curvature on the input impedance and resonant frequency of both a doubly curved conformal square and circular patch with various orientations and probe feed positions were investigated. The technique presented in this paper will serve as a useful tool in the design and analysis of doubly curved microstrip patch antennas.

REFERENCES

1. Wong, K.-L., *Design of Nonplanar Microstrip Antennas and Transmission Lines*, Wiley, 1999.
2. Macon, C. A., L. C. Kempel, and S. W. Schneider, "Radiation and scattering by complex conformal antennas on a circular cylinder," *Adv. in Comp. Math.*, Vol. 16, 191–209, April 2002.
3. Macon, C. A., L. C. Kempel, K. Trott, and S. W. Schneider, "Conformal multi-modal antennas on cylinders," *Millennium Conference on Antennas and Propagation*, Davos, Switzerland, April 2000.
4. Garg, R., P. Bhartia, I. Bahl, and A. Ittipiboon, *Microstrip Antenna Design Handbook*, Artech House, 2001.
5. Schultz, F. V., "Scattering by a prolate spheroid," Ph.D. Dissertation, University of Michigan, Ann Arbor, Michigan, 1950.
6. Li, L.-W., M.-S. Leong, P.-S. Kooi, and T.-S. Yeo, "Spheroidal vector wave eigenfunction expansion of dyadic Green's functions for a dielectric spheroid," *IEEE Trans. Antennas and Propagat.*, Vol. 49, No. 4, April 2001.
7. Spence, R. D. and C. P. Wells, "Vector wave functions," *Symposium on the Theory of Electromagnetic Waves*, Michigan State College, June 1950.
8. Sinha, B. P. and R. H. MacPhie, "Electromagnetic scattering by prolate spheroids for plane waves with arbitrary polarization and

angle of incidence," *Radio Science*, Vol. 12, No. 2, March–April 1977.

9. Tai, C.-T., *Dyadic Green Functions in Electromagnetic Theory*, IEEE Press, 1994.
10. Volakis, J. L., A. Chatterjee, and L. C. Kempel, *Finite Element Method for Electromagnetics with Application to Antennas, Microwave Circuits, and Scattering*, IEEE Press, 1998.
11. Pathak, P. H. and N. N. Wang, "An analysis of the mutual coupling between antennas on a smooth convex surface," Tech. Report 784583-7, ElectroScience Laboratory, Ohio State University, 1978.
12. Macon, C. A., "Modeling the radiation from cavity-backed antennas on prolate spheroids using a hybrid finite element-boundary integral method," Ph.D. Dissertation, Michigan State University, East Lansing, Michigan, 2001.
13. Jin, J.-M., *The Finite Element Method in Electromagnetics*, Wiley-Interscience, 1993.
14. Josefsson, L. and P. Persson, "An analysis of mutual coupling on doubly curved convex surfaces," *2001 IEEE APS Int. Symp. Dig.*, Vol. 2, 342–345, Boston, MA, 2001.
15. Kempel, L. C. and K. Trott, "Progress in modeling complex conformal antennas using the finite element-boundary integral method," *1998 URSI Radio Science Meeting*, Atlanta, GA, June 1998.